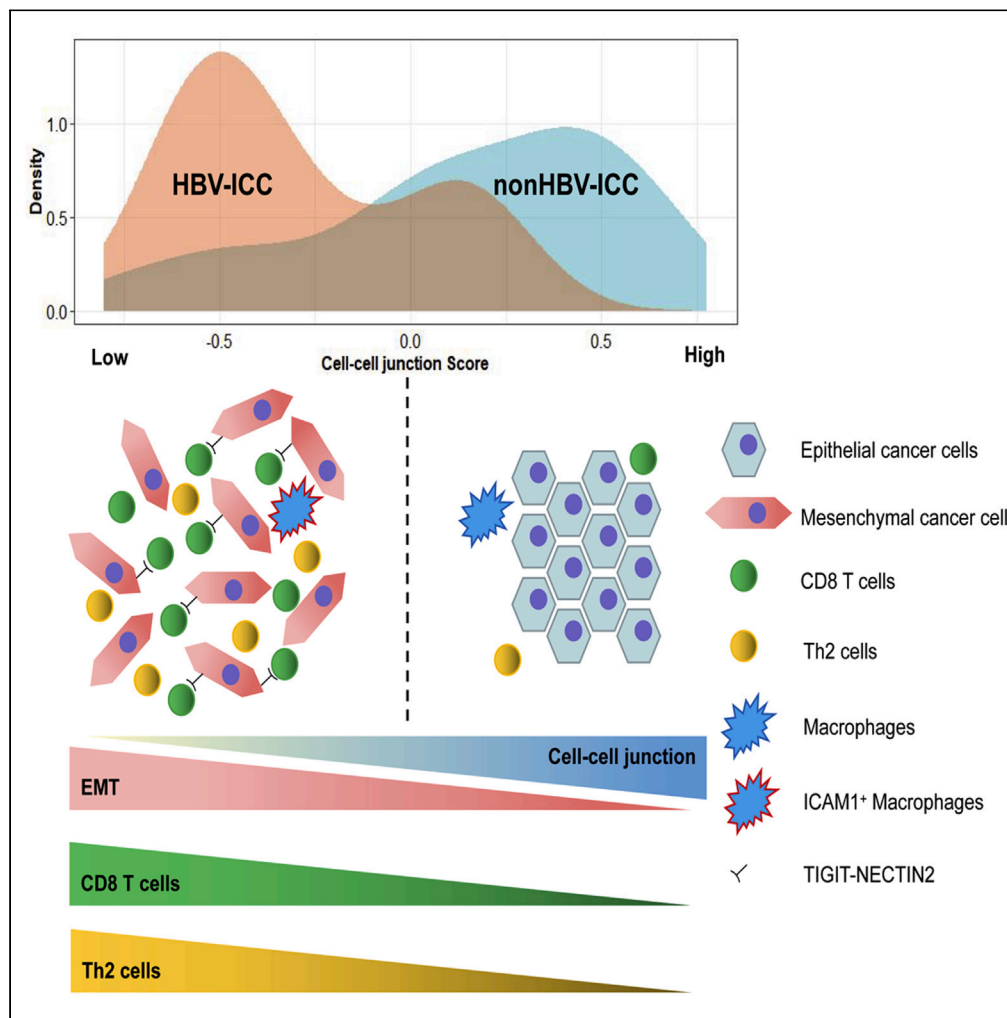## Article

Proteomic and single-cell landscape reveals novel pathogenic mechanisms of HBV-infected intrahepatic cholangiocarcinoma

Yifei Shen, Shuaishuai Xu, Chanqi Ye, ..., Michael P. Timko, Peng Zhao, Jian Ruan

mpt9g@virginia.edu (M.P.T.)
zhaop@zju.edu.cn (P.Z.)
software233@zju.edu.cn (J.R.)

Highlights

Multiomics reveals EMT program changes increased in tumor cells of HBV-ICC patients

ICAM1[+] TAMs are correlated with a poor prognosis in HBV-ICC patients

Single-cell analysis indicated the immunosuppressive landscape in HBV-ICC patients

Article

Proteomic and single-cell landscape reveals novel pathogenic mechanisms of HBV-infected intrahepatic cholangiocarcinoma

Yifei Shen,[1,2,9] Shuaishuai Xu,[3,9] Chanqi Ye,[3,9] Qiong Li,[3,9] Ruyin Chen,[3,9] Wei Wu,[3] Qi Jiang,[3] Yunlu Jia,[3] Xiaochen Zhang,[3] Longjiang Fan,[4] Wenguang Fu,[5] Ming Jiang,[6] Jinzhang Chen,[7] Michael P. Timko,[8,*] Peng Zhao,[3,*] and Jian Ruan[3,10,*]

SUMMARY

Despite the epidemiological association between intrahepatic cholangiocarcinoma (ICC) and hepatitis B virus (HBV) infection, little is known about the relevant oncogenic effects. A cohort of 32 HBV-infected ICC and 89 non-HBV-ICC patients were characterized using whole-exome sequencing, proteomic analysis, and single-cell RNA sequencing. Proteomic analysis revealed decreased cell-cell junction levels in HBV-ICC patients. The cell-cell junction level had an inverse relationship with the epithelial-mesenchymal transition (EMT) program in ICC patients. Analysis of the immune landscape found that more CD8 T cells and Th2 cells were present in HBV-ICC patients. Single-cell analysis indicated that transforming growth factor beta signaling–related EMT program changes increased in tumor cells of HBV-ICC patients. Moreover, ICAM1$^+$ tumor-associated macrophages are correlated with a poor prognosis and contributed to the EMT in HBV-ICC patients. Our findings provide new insights into the behavior of HBV-infected ICC driven by various pathogenic mechanisms involving decreased cell junction levels and increased progression of the EMT program.

INTRODUCTION

Intrahepatic cholangiocarcinoma (ICC) is the second-most-common primary liver cancer with increasing incidence and mortality worldwide.[1,2] Data show that the incidence of ICC and ICC-related mortality rates have been rapidly increasing globally over recent decades.[3] While the etiology and pathogenesis are still not fully understood, the risk factors are gradually being established. Currently, the risk factors associated with ICC mainly consist of ICC-specific risk factors, represented by bile-duct-related diseases including bile duct stones or cysts and primary sclerosing cholangitis, and shared risk factors with hepatocellular carcinoma (HCC) including liver fluke parasites, chronic hepatitis B virus (HBV) or hepatitis C virus infection, and certain toxins.[4] ICC is associated with low survival rates, and surgical resection is the only potentially curative intervention for ICC.[5] Unfortunately, ICC patients are typically diagnosed late in the disease state, and the tumors are most often unresectable at the time of diagnosis, leaving conservative medicine as the only option, which remains limited.

The epidemiological linkage between HBV and HCC or ICC is well established, and earlier studies have explored HCC genomic alterations and identified HBV-associated driver mechanisms involved in hepatocarcinogenesis.[6–8] Several studies have identified the genomic architecture of HBV-infected ICC tumors.[9–12] However, the relationship between HBV infection and ICC pathogenesis is not well characterized at the gene expression level. Thus, a systematic and deeper understanding of HBV-ICC is required to elucidate its pathogenesis and identify potential therapeutic strategies. Traditionally, investigations were mainly performed at the bulk-tumor level and have inherent limitations in providing precise information on individual cells residing in a highly admixed tumor microenvironment (TME). Single-cell sequencing provides an important advancement for the study of cancers.[13] In this regard, only a very limited number of studies of ICC have been carried out using single-cell analyses.

To dissect the pathogenic mechanisms in HBV-ICC, we systematically analyzed the genomic and proteomic features and tumor immune environment of HBV-ICC (Figure 1A). In addition, we took advantage of the unique

[1]Department of Laboratory Medicine, The First Affiliated Hospital, Zhejiang University School of Medicine, Hangzhou 310000, Zhejiang Province, People's Republic of China

[2]Key Laboratory of Clinical In Vitro Diagnostic Techniques of Zhejiang Province, Hangzhou 310000, Zhejiang Province, People's Republic of China

[3]Department of Medical Oncology, The First Affiliated Hospital, Zhejiang University School of Medicine, & Key Laboratory of Cancer Prevention and Intervention, Ministry of Education, Hangzhou 310000, Zhejiang Province, People's Republic of China

[4]Institute of Bioinformatics, Zhejiang University, Hangzhou 310000, Zhejiang Province, People's Republic of China

[5]Department of Hepatobiliary Surgery, The Affiliated Hospital of Southwest Medical University, Luzhou 646000, Sichuan Province, People's Republic of China

[6]The Children's Hospital, Zhejiang University School of Medicine and National Clinical Research Center for Child Health, Hangzhou 310058, Zhejiang Province, People's Republic of China

[7]Department of Oncology, Nanfang Hospital, Southern Medical University, Guangzhou 510000, Guangdong Province, People's Republic of China

[8]Departments of Biology and Public Health Sciences, University of Virginia, Charlottesville, VA 22904, USA

Continued
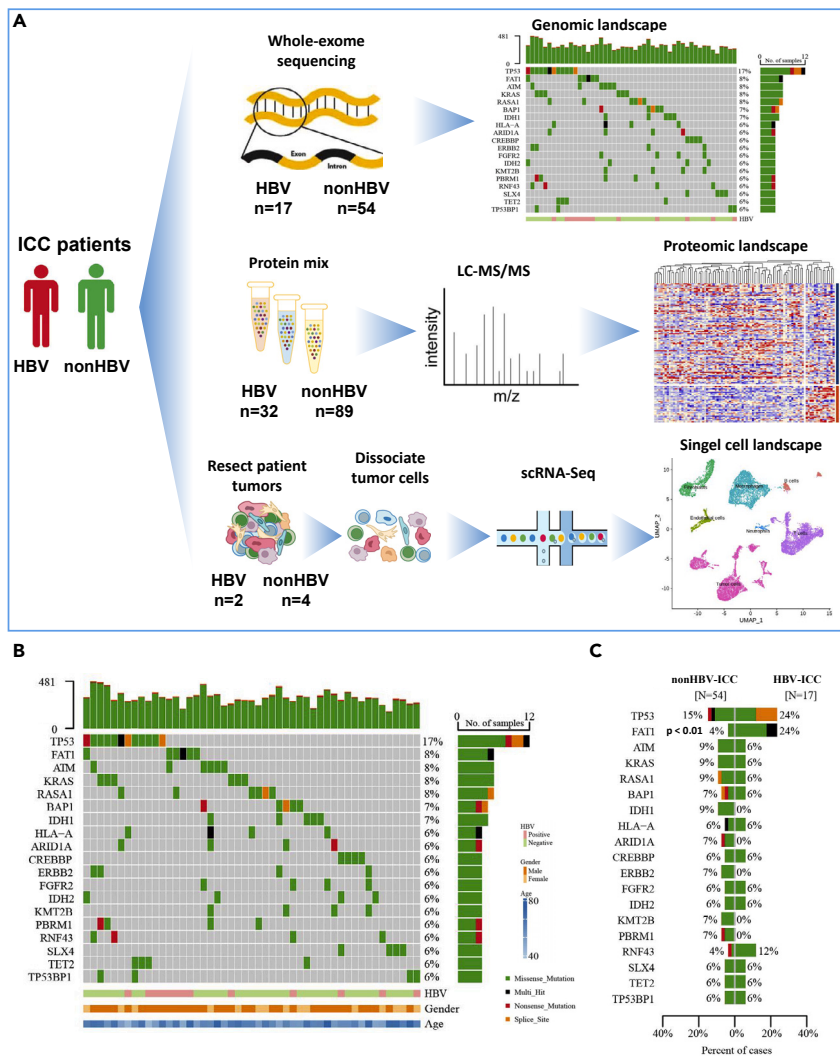
Figure 1. The genomic landscape of HBV-ICC and non-HBV-ICC

(A) Overview of the experiment design.

(B) Significantly mutated genes in ICC patients.

(C) Differentially mutated genes between HBV-ICC and non-HBV-ICC patients.

multidimensional capacity of single-cell RNA sequencing (scRNA-seq) to delineate the multifaceted landscapes and cell-cell interactions in HBV-ICC. Our studies found that the behavior of HBV-infected ICC is driven by various pathogenic mechanisms involving decreases in cell-cell junction levels, increases in the epithelial-mesenchymal transition (EMT) program, and alterations in the immunosuppressive environment. These findings allowed the identification of specific molecular targets for subsequent translational applications and provided useful mechanistic information for the design of efficacious immune-oncology treatments in ICC.

RESULTS

Somatic mutation characteristics in HBV-ICC and non-HBV-ICC

To genetically characterize HBV-ICC and non-HBV-ICC, we performed whole-exome sequencing on 17 HBV-ICC and 54 non-HBV-ICC patients with a minimum of 20-fold coverage. We analyzed the whole-exome sequencing (WES) data and identified 18,262 somatic synonymous and nonsynonymous mutations (including single-nucleotide mutations and small insertions and deletions). The predominant somatic mutation type was C:G > T:A transitions. Recurrent missense mutations in TP53 were observed in 12 of 71 (17%) patients (Figure 1B). These mutations all impaired the DNA-binding domain of the TP53 protein, similar to

[9]These authors contributed equally

[10]Lead contact

*Correspondence:
mpt9g@virginia.edu (M.P.T.),
zhaop@zju.edu.cn (P.Z.),
software233@zju.edu.cn (J.R.)
https://doi.org/10.1016/j.isci.2023.106003

Figure 2. Proteomic analysis revealed decreased cell-cell junction level in HBV-ICC patients

(A) Heatmap of DEGs expression level in HBV-ICC and non-HBV-ICC patients. (row: genes, column: patients).

(B) Volcano plot of DEGs between HBV-ICC and non-HBV-ICC patients. (green: higher in non-HBV-ICC; red: higher in HBV-ICC).

(C) GO enrichment analysis results based on DEGs.

(D) GSVA score of the cell junction-related pathways in HBV-ICC and non-HBV-ICC patients. Data are represented as medians and interquartile ranges.

(E) Heatmap of cell junction-related gene expression level.

(F) Cell-cell junction score (CCJ score) in HBV-ICC and non-HBV-ICC patients. Data are represented as medians and interquartile ranges.

(G) Survival analysis in ICC patients with low and high CCJ scores based on datasets generated in this study.

(H) Survival analysis in low- and high-CCJ-score ICC patients based on the TCGA ICC RNA-Seq dataset.

what has been frequently observed in ICC.[9,11] FAT1, ATM, KRAS, and RASA1 were the second most affected genes in six (8%) patients. In addition, five mutations were found in BAP1 and IDHA1, and four mutations were found in each of the following genes: HLA-A, ARID1A, CREBBP, ERBB2, FGFR2, IDH2, KMT2B, PBRM1, RNF43, SLX4, TET2, and TP53BP1 (Figure 1B). To further investigate the differences between HBV-ICC and non-HBV-ICC patients, we compared HBV-ICC and non-HBV-ICC cohorts to detect differentially mutated genes (Figure 1C). We performed Fisher exact test on all genes between the two cohorts to detect differentially mutated genes. Interestingly, among all genes, we found FAT1 had a significantly higher mutation rate in HBV-ICC patients (24%) than in non-HBV-ICC patients (4%). It was recently reported that in mouse models and human cancers, FAT1 deletion promotes the acquisition of a hybrid EMT state presenting increased tumor stemness and metastasis.[14]

Proteomic analysis revealed decreased cell-cell junction level in HBV-ICC

To further characterize the molecular features of the HBV-ICC tumors, ICC tissues derived from 121 patients (HBV-ICC n = 32, non-HBV-ICC n = 89) were procured for proteomics analysis (Figure 2A). A total of 10,888 proteins were identified and quantified with low batch variance. Differentially expressed protein (DEP) analysis was performed on data from HBV-ICC and non-HBV-ICC patients (Figure 2B). Eighty-six genes were identified to have significantly changed between HBV-ICC and non-HBV-ICC patients. Among the 86 genes, 84% (72/86) were downregulated, and 16% (14/86) were upregulated in the HBV-ICC. We further used the DEPs to perform gene ontology (GO) enrichment analysis and found the GO function terms related with cell junction organization (i.e., "desmosome organization" and "cell-cell junction organization") were significantly enriched in the DEPs (Figure 2C). We next conducted the gene set enrichment analysis (GSEA) based on the total detected genes using the REACTOME pathway database. The results of this analysis also revealed that cell junction organization-related pathways (i.e., "tight junction interaction" and "adherens junction interaction") were significantly downregulated in HBV-ICC patients compared to those in non-HBV-ICC patients (Figure 2D). Based on the DEP enrichment analysis and GSEA results, proteomic analysis revealed decreased cell-cell junction level in HBV-ICC. We further performed a stepwise logistic regression to detect the marker gene sets to distinguish HBV-ICC and non-HBV-ICC based on cell junction-related genes.[15] A gene set that included 8 genes (TJP1, CTNNA1, CTNNB1, CD9, PKP3, DSP, JUP, DSG2) was identified in the analysis (Figure 2E). Based on the gene set, we calculated the cell-cell junction score (CCJ score) based on the gene set variation analysis (GSVA) analysis in each sample. The CCJ score could discriminate the HBV-ICC and non-HBV-ICC patients successfully (Figure 2F). To further investigate the relationship between cell junction level and survival rates of ICC patients, we performed a survival analysis between low- and high-CCJ-score ICC patient groups. The results showed that patients with low CCJ scores had significantly lower survival rates (p < 0.05) (Figure 2G). We next applied the CCJ score on the 30 The Cancer Genome Atlas (TCGA) ICC patients. The results of this analysis also showed that ICC patients with low CCJ scores had lower survival rates than patients with high CCJ scores (Figure 2H).

The inverse relationship between cell-cell junction level and EMT program in ICC patients

It was previously reported that the first step of EMT is the disassembly of epithelial cell-cell contacts (i.e., tight junctions [TJ], adherens junctions [AJ], desmosomes, and gap junctions).[16] To further investigate the relationship between the levels of cell-cell junctions and EMT in ICC, we compared the gene expression level of the EMT biomarkers CDH1 (E-cadherin) and CTNNB1 (beta-catenin) in HBV-ICC and non-HBV-ICC patients. The expression of these two biomarker genes was previously reported to decrease during the EMT process.[17] The results showed that the gene expression of CDH1 and CTNNB1 was significantly decreased in HBV-ICC patients compared to that in non-HBV-ICC patients (Figure 3A), suggesting a more rapid EMT in HBV-ICC patients. To further dissect whether the epithelial cell proportion decreased during the EMT in an HBV-ICC patient, we calculated epithelial cell abundance based on a deconvolution method "xCell" using the proteomic
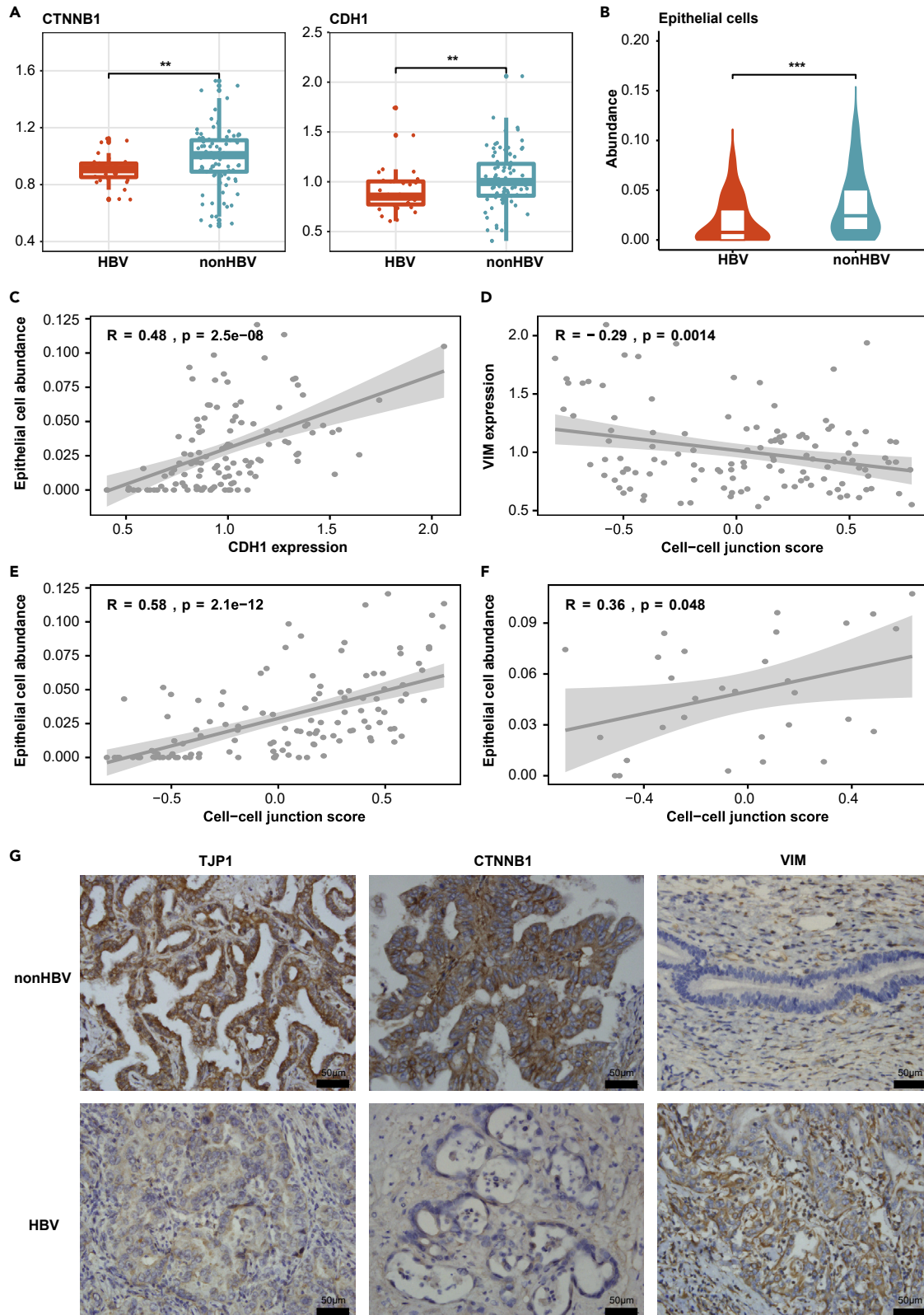
Figure 3. The inverse relationship between cell-cell junction level and EMT program in ICC patients

(A) Gene expression level of the EMT biomarkers (*CDH1*, *CTNNB1*) in HBV-ICC and non-HBV-ICC patients. Data are represented as medians and interquartile ranges.

(B) Epithelial cell abundance in HBV-ICC patients and non-HBV-ICC patients. Data are represented as medians and interquartile ranges.

(C) The relationship between epithelial cell abundance and *CDH1* expression level.

(D) The relationship between CCJ score and *VIM* expression level.

(E) The relationship between CCJ score and epithelial cell proportion in our dataset.

(F) The relationship between CCJ score and epithelial cell proportion in TCGA datasets.

(G) Immunohistochemistry of cell junction and EMT-related proteins TJP1, CTNNB1, and VIM in representative HBV-HCC and non-HBV-ICC patients. Scale bars, 50 μm. More than five fields each under 40× and 100× magnification were examined.

dataset. The results of this analysis revealed that epithelial cell abundance was significantly lower in HBV-ICC patients than in non-HBV-ICC patients (Figure 3B). The relationship analysis revealed the decrease of epithelial cell abundance was related with decreasing CDH1 expression level (increasing EMT) in HBV-ICC patients (p < 0.01) (Figure 3C). Vimentin (VIM) is a gene that encodes the intermediate filament protein, which is characteristically upregulated in cells undergoing EMT. To further investigate the relationship between the cell junction level and EMT program, we performed a correlation analysis between CCJ score and the VIM gene expression level. The results showed that the CCJ score was significantly negatively correlated with the VIM expression level (R = −0.29, p < 0.01) (Figure 3D), which suggested the inverse relationship between cell-cell junction levels and the EMT program in ICC patients. To further validate whether the epithelial cell proportion decreased in ICC patients with a low cell-cell junction level, we conducted a correlation analysis between the CCJ score and epithelial cell proportion in our ICC patients and TCGA ICC patients. The results indicated that the cell junction level was significantly positively correlated with epithelial cell proportion in both our ICC (p < 0.01) (Figure 3E) and TCGA ICC (p < 0.05) datasets (Figure 3F). Furthermore, we observed greater expression of VIM and less expression of TJP1 and CTNNB1 in HBV-ICC patients based on immunohistochemistry (IHC) staining (Figure 3G).
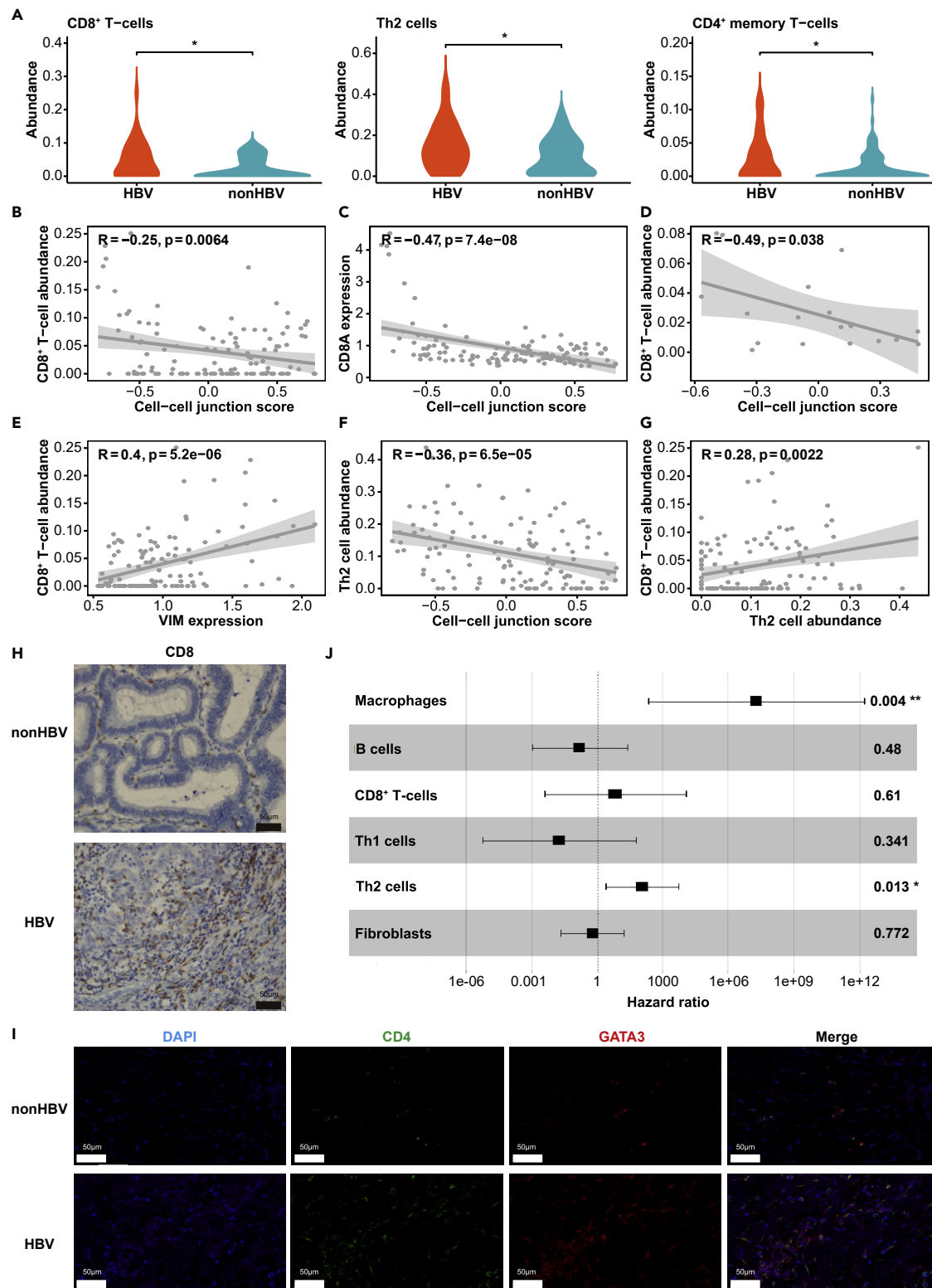
More CD8 T cells and Th2 cells were found in HBV-ICC patients

We next dissected the immune landscape differences between HBV-ICC and non-HBV-ICC. The relative abundance of 16 immune cell types was estimated by the "xCell" method based on the ICC proteomic dataset. A significantly greater abundance of CD8 T cells, Th2 cells, and CD4 memory T cells were found in HBV-ICC patients than in non-HBV-ICC patients (Figure 4A). To further investigate the relationship between CD8 T cell abundance and cell-cell junction levels, we performed a correlation analysis between CD8 T cell abundance and CCJ score. The results showed that CD8 T cell abundance had significantly inverse relationship with cell-cell junction levels (p < 0.01) (Figure 4B). To validate these results, we performed a correlation analysis between the CD8 T cell marker gene (CD8A) and CCJ score (Figure 4C). The results of this analysis provided further support for the observed inverse correlation between cell-cell junction level and CD8 T cell abundance (p < 0.01). In addition, we found an inverse relationship between cell-cell junction level and CD8 T cell abundance in TCGA ICC patients (p < 0.05) (Figure 4D). Interestingly, VIM expression level was also observed to be significantly positively correlated with CD8 T cell abundance (Figure 4E). A correlation analysis between CCJ score and Th2 cell abundance was also found that Th2 cell abundance had a significant inverse correlation with cell-cell junction level (p < 0.01) (Figure 4F), whereas Th2 cell abundance was significantly positively correlated with CD8 T cell abundance (Figure 4G). These results suggested that HBV-ICC patients with low cell-cell junction levels and more EMT transition will have more CD8 T cells and Th2 cells. In addition, we observed more CD8 cells in HBV-ICC patients based on IHC staining (Figure 4H). We also observed more Th2 cells in HBV-ICC patients using multicolor immunofluorescence staining (Figure 4I).

To investigate the clinical role of the immune cell types identified in the present study, we performed Cox regression analysis based on the cell type abundance and overall survival (OS) of ICC patients (Figure 4J). Strikingly, we found that the accumulation of macrophages and Th2 cells was related to poorer OS. Also of note, we found that the proportion of CD8 T cells present was not correlated with OS of the ICC patients, suggesting that cytotoxicity of CD8 T cells might be suppressed in the HBV-ICC patients. Further single-cell analysis confirmed that CD8 T cells were immunosuppressive in HBV-ICC patients, and higher expression levels of immune checkpoints were found in the CD8 T cells of HBV-ICC patients (Figure 7).

A single-cell transcriptome map of HBV-ICC and non-HBV-ICC

To further investigate changes in the cancer cells and tumor-infiltrating lymphocytes between HBV-ICC and non-HBV-ICC patients, we performed scRNA-seq experiments using samples from six ICC patients (two

Figure 4. More CD8 T cells and Th2 cells were found in HBV-ICC patients

(A) Cell type abundance of CD8 T cells, Th2 cells, and CD4 memory T cells in HBV-ICC and non-HBV-ICC patients.

(B) The relationship between CD8 T cell abundance and CCJ score.

(C) The relationship between CD8A expression level and CCJ score.

Figure 4. *Continued*
(D) The relationship between CD8 T cell abundance and CCJ score in the TCGA dataset.
(E) The relationship between CD8 T cell abundance and VIM expression level.
(F) The relationship between Th2 cell abundance and CCJ score.
(G) The relationship between CD8 T cell abundance and Th2 cell abundance.
(H) Immunohistochemistry of CD8 T cells in representative HBV-HCC and non-HBV-ICC patients. Scale bars, 50 μm.
(I) Representative immunofluorescent images of GATA3$^+$CD4$^+$ T cells (Th2 cells) in HBV-ICC and non-HBV-ICC patients. Scale bars, 50 μm. More than five fields were examined for each sample under 40× and 100× magnification.
(J) Association between relative cell abundance and patient survival (Cox regression analysis). Data are represented as hazard ratio and 95% confidence intervals.

HBV-ICC patients and four non-HBV-ICC patients). Using the cleaned dataset derived from the six clinical ICC patients, we conducted a principal component analysis using the most highly variable genes and computed the linear dimension reduction on the first 100 principal components (PCs). Considering the PC heatmap and PC elbow plot, we included the first 30 PCs in subsequent analyses. To visualize these data, we applied a uniform manifold approximation and projection (UMAP) algorithm[18] to perform nonlinear dimensionality reduction. The single cells were stratified according to their global transcriptomic landscape in two-dimensional space, indicating their gene expression similarity/difference (Figure 5A). The results indicated that some cell clusters contained single cells from multiple patients, while others consisted of cells primarily from one individual. On examining the expression of cell-type markers, tumor markers, and copy number variation (CNV) in the single cells, the cell type identity was determined (Figure 5B). We found that malignant and nonmalignant cells clustered into distinct cell clusters, with malignant cells (tumor cells) from different patients separated into different cell clusters while nonmalignant cells from multiple patients admixed together (Figure 5A). We further calculated the proportion of each cell type among all the cells. The results showed that HBV-ICC patients had more CD8 T cells than non-HBV-ICC patients (Figure 5C), a finding consistent with the immune landscape analysis based on the proteomic dataset (described above).
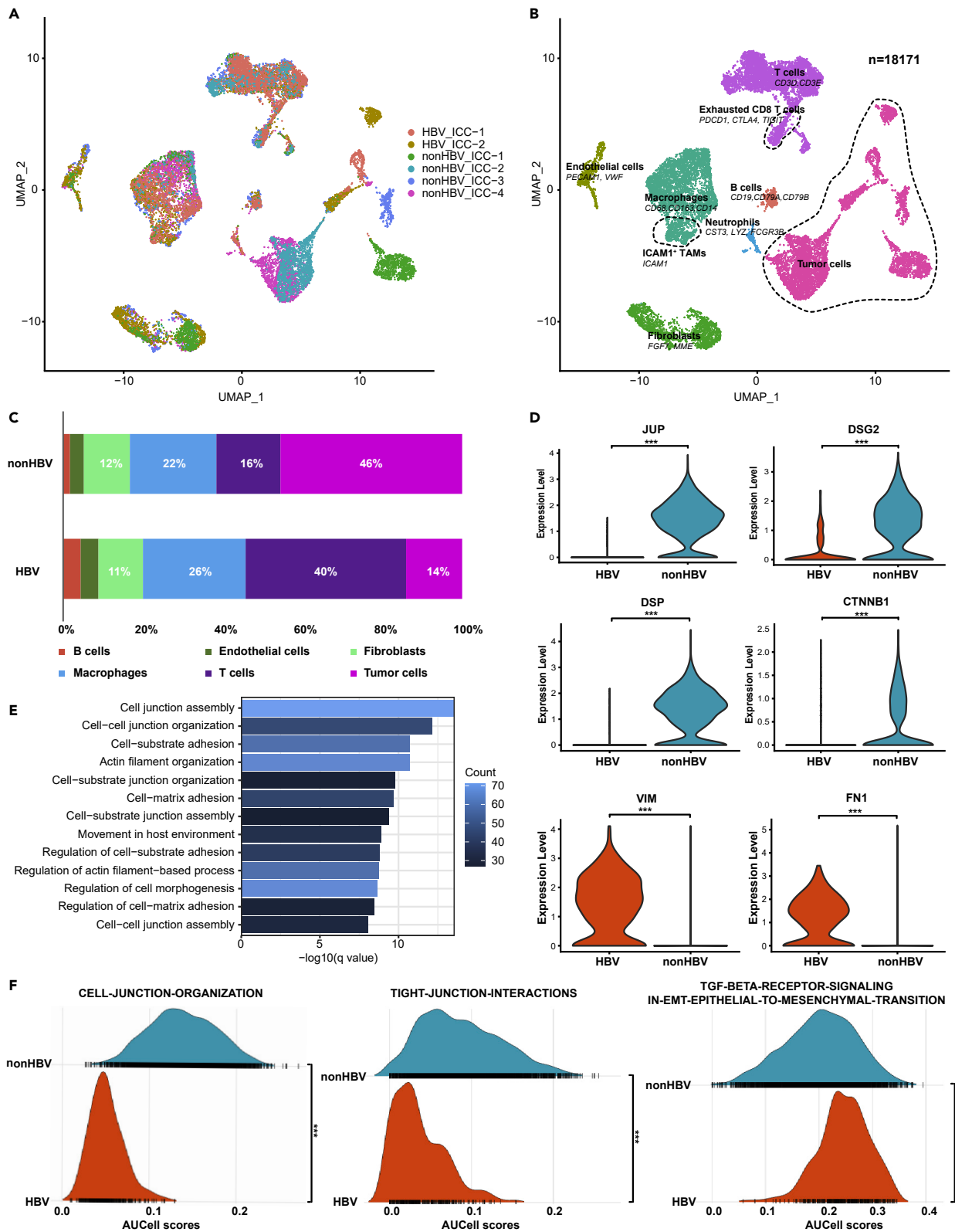
Transforming growth factor beta signaling–related EMT program increased in tumor cells of HBV-ICC

To dissect the differences between HBV-ICC and non-HBV-ICC tumor cells, we first analyzed the genes differentially expressed in the tumor cells in HBV-ICC and non-HBV-ICC patients. Among the differentially expressed genes (DEGs), cell junction-related genes (e.g., JUP2, DSG2, DSP, CTNNB1) were significantly downregulated in the HBV-ICC tumor cells compared to those in non-HBV-ICC tumor cells (Figure 5D). This observation suggested decreased cell-cell junction levels in the HBV-ICC patients and coincided with what we found in the proteomic dataset. We further used the DEGs to perform a GO enrichment analysis. The GO function terms related with cell-cell junction organization (i.e., "cell junction assembly" and "cell-cell junction organization") were significantly enriched in the DEGs (Figure 5E). In addition, the expression level of EMT biomarker genes (i.e., VIM, FN1) were found to be significantly upregulated in the HBV-ICC tumor cells (Figure 5D), suggesting faster progression of EMT-related activity in the HBV-ICC tumor cells.

To further investigate the pathways differing between the HBV-ICC and non-HBV-ICC tumor cells, we conducted GSEA using "AUCell" based on the REACTOME pathway database. The results again showed that cell-cell junction-related pathways such as "cell junction organization" and "tight junction interaction" were significantly downregulated in the HBV-ICC tumor cells (Figure 5F). In contrast, transforming growth factor beta (TGFβ)-signaling-related pathways associated with EMT (i.e., "TGFβ-signaling," "epithelial mesenchymal transition," and "TGFβ-receptor signaling in EMT transition") were significantly upregulated in tumor cells of HBV-ICC patients (Figure 5F) suggesting that TGFβ-signaling is important in driving the EMT transition increase in the HBV-ICC patients.

ICAM1$^+$ tumor-associated macrophages are correlated with a poor prognosis in HBV-ICC patients

To further understand the differences of tumor-infiltrating immune cells between HBV-ICC and non-HBV-ICC, we next focused on the tumor-associated macrophages (TAMs) in the ICC TME because TAMs were found to be a major immune cell type (Figure 5C) and significantly correlated with prognosis (Figure 4J) in the ICC patients.

Figure 5. scRNA-seq Suggests cell-cell junction level decreased and TGFβ-signaling-related EMT program increased in tumor cells of HBV-ICC

(A and B) UMAP plot of single cells profiled in the presenting work colored by patient (A) and major cell types (B).

(C) Summary of the different major cell types identified in HBV-ICC and non-HBV-ICC patients.

(D) Expression level of cell junction-related genes and EMT biomarker genes in tumor cells in HBV-ICC and non-HBV-ICC patients.

(E) GO enrichment analysis results based on DEGs between HBV-ICC and non-HBV-ICC tumor cells.

(F) Comparison of pathway analysis results between HBV-ICC and non-HBV-ICC tumor cells.

Interestingly, we found that intercellular adhesion molecule-1 (ICAM1), one of the most significantly upregulated genes in the HBV-ICC patients in the proteomic dataset, was expressed in the TAMs rather than tumor cells (Figure 6A). Survival analysis revealed that a high ICAM1 expression level was correlated with poor prognosis in the ICC patients (Figure 6B). Additionally, the results of single-cell analysis showed that ICAM1 was significantly upregulated in the HBV-ICC TAMs compared with non-HBV-ICC TAMs (Figures 6C and 6D). This observation is consistent with ICAM1 upregulation in HBV-ICC patients in the proteomic dataset. We also observed frequent overlap of the ICAM1 and macrophages (CD68) in HBV-ICC patients using multicolor immunofluorescence staining (Figure 6E). In addition, we found the expression level of ICAM1 had a significant inverse correlation with the CCJ score in proteomic data (Figure 6F), suggesting that the increased ICAM1 expression level in macrophages was related to decreasing cell-cell junction level in the tumor cells of HBV-ICC patients. Having found that TGFβ-signaling-related EMT program was increased in tumor cells of HBV-ICC patients, we further dissected the expression level of TGFB1 among all the cells. Strikingly, the TGFB1 expression level was significantly increased in the HBV-ICC TAMs compared to non-HBV-ICC TAMs (Figures 6H and 6I). Further correlation analysis indicated that TGFB1 and ICAM1 were significantly coexpressed in TAMs (p < 0.01). The results implied that ICAM1+ TAMs contribute to the EMT through TGFβ-signaling pathways in HBV-ICC.

To understand the involvement of cellular status in the TAMs, we derived the pseudotime cell trajectory of the TAMs in HBV-ICC patients (Figure 6J). LAIR1 (CD305) is a transmembrane glycoprotein[19] constitutively expressed on most mononuclear leukocytes[20,21] and some cancer cells.[22,23] Cross-linking of LAIR1 on the surface of immune cells causes inhibitory functions.[24] Interestingly, in the proteomic datasets, we found a significantly positive correlation between LAIR1 and ICAM1 gene expression levels (Figure 6G). Further examination of ICAM1 and LAIR1 expression levels using the pseudotime cell trajectory analysis showed that ICAM1 and LAIR1 expression levels increased during TAMs' transition toward a more immunosuppressive state (Figure 6K). The results suggested that ICAM1+ TAMs were a subset of immunosuppressive TAMs.

The immunosuppressive landscape of CD8 T cell immune checkpoints in HBV-ICC patients

Immune checkpoints function as "brakes" on T cell immune responses, resulting in the weakening of T cell attack and immune tolerance/escape. In our proteomic analysis results, we found that the proportion of CD8 T cells present in the HBV-ICC patients was increased. However, there is no significant relationship between the CD8 T cell proportion and prognosis. To further investigate whether the CD8 T cell was immunosuppressive in HBV-ICC patients, we examined the expression of immune checkpoint components in both tumor-infiltrating immune cells (i.e., CD8 T cells) and complementary antigen-presenting cells (APCs) (i.e., tumor cells). Interestingly, we found that PDCD1 (PD-1) and TIGIT (T cell immunoreceptor with Ig and ITIM domains) had higher expression levels in the CD8 T cells of HBV-ICC patients (Figure 7A), and NECTIN2 (nectin cell adhesion molecule 2) had higher expression levels in tumor cells of HBV-ICC patients (Figure 7B). We also observed more NECTIN2 and TIGIT in HBV-ICC patients based on IHC staining (Figure 7C). Through pseudotime analyses, we observed the gradual transition of CD8 T cells toward the subpopulations with exhaustion status in HBV-ICC patients (Figure 7D). Such exhaustion status for CD8 T cells was indicated by the upregulation of PDCD1 and TIGIT (Figure 7E). On evaluating the cell-cell interaction status based on "CellPhoneDB," we estimated the relative contribution of different coinhibitory checkpoints in shaping the immunosuppressive landscape in HBV-ICC (Figure 7F). We identified a prominent coinhibitory signal via the TIGIT-NECTIN2 axis in complementary T cells and tumor cells. NECTIN2 (also called PVRL2) was the most highly expressed gene in the PVR gene family in these patients.

DISCUSSION

In this study, we systematically performed the genomic, proteomic, and single-cell transcriptomic analyses of HBV-ICC and non-HBV-ICC in order to dissect the pathogenic mechanisms in HBV-ICC. Based on the genomic
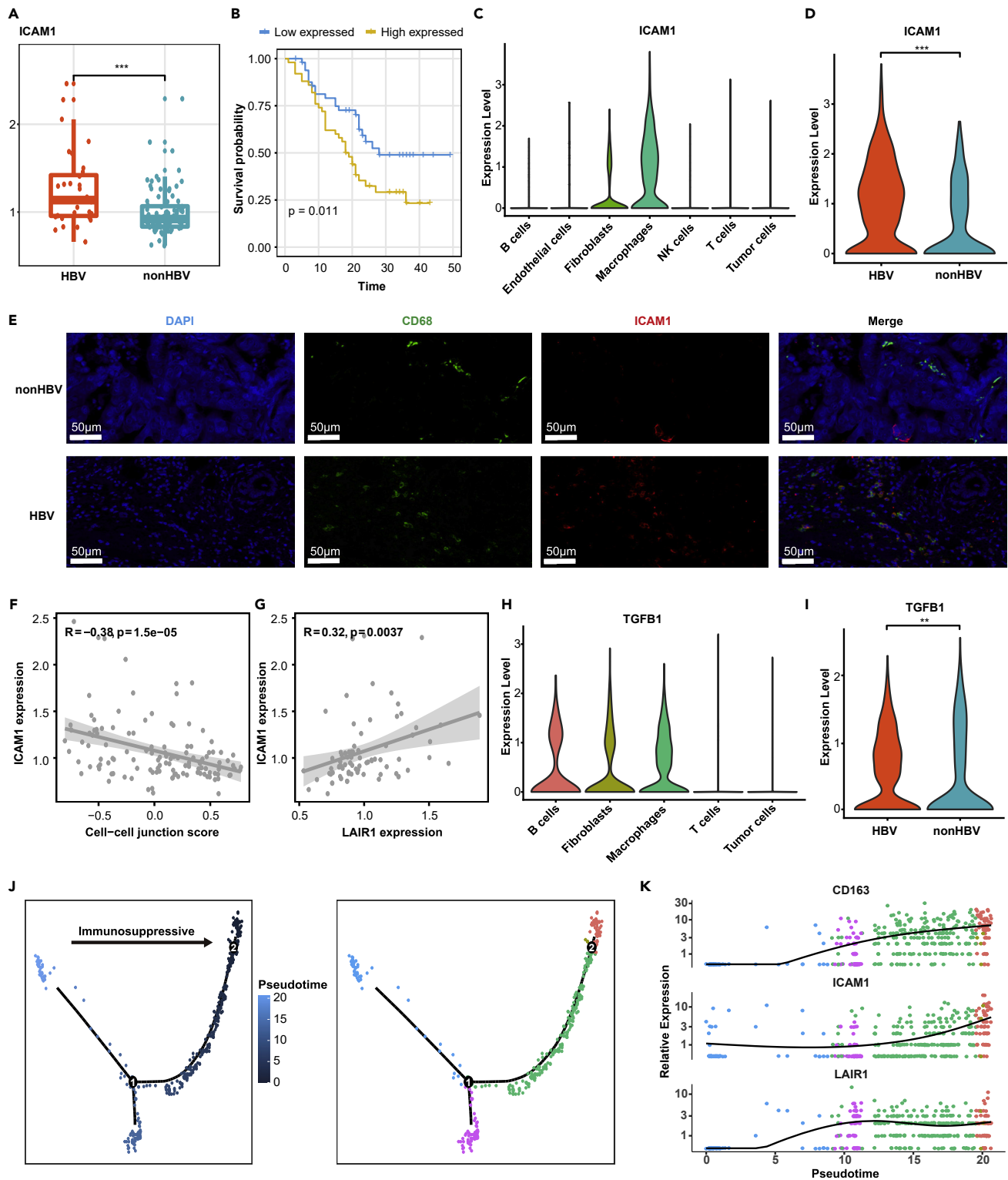
Figure 6. ICAM1⁺ TAMs are correlated with a poor prognosis in HBV-ICC

(A) *ICAM1* expression level in HBV-ICC and non-HBV-ICC. Data are represented as medians and interquartile ranges.

(B) Survival analysis between low- and high-*ICAM1*-expressed ICC patients.

(C) *ICAM1* expression level in major cell types in ICC patients.

(D) *ICAM1* expression level in macrophages of HBV-ICC and non-HBV-ICC patients.

Figure 6. Continued
(E) Overlap of the ICAM1 and macrophages (CD68) using multicolor immunofluorescence staining in HBV-ICC and non-HBV-ICC patients. Scale bars, 50 μm.
(F) The relationship between CCJ score and ICAM1 expression level.
(G) The relationship between *LAIR1* and *ICAM1* expression level.
(H) *TGFB1* expression level in major cell types in ICC patients.
(I) *TGFB1* expression level in macrophages of HBV-ICC and non-HBV-ICC patients.
(J) Pseudotime cell trajectory analysis on TAMs in HBV-ICC samples.
(K) Expression levels of *CD163*, *ICAM1*, and *LAIR1* genes in TAMs along pseudotime.

analysis, we found that FAT1 had a significantly higher mutation rate in HBV-ICC patients than in non-HBV-ICC patients. A recent study using mouse models and analysis of human cancers found that FAT1 deletion promotes the acquisition of a hybrid EMT state that presents increased tumor stemness and metastasis.[14] They also found that the epigenetic and transcriptional mechanisms that link a loss of cell polarity and cell adhesion with the induction of a hybrid EMT phenotype occur downstream of the FAT1 deletion.[14]

To further investigate whether the EMT state changes during ICC development, we performed a proteomic analysis in HBV-ICC and non-HBV-ICC patients. Our proteomic analysis revealed that HBV-ICC had decreased cell-cell junction levels and that an inverse relationship existed between cell-cell junction level and EMT program in ICC patients. The ability of epithelial cells to organize through cell-cell adhesion into a functioning epithelium serves the purpose of a tight epithelial protective barrier. Contacts between adjacent cells are made up of TJ, AJ, and desmosomes with unique cellular functions and a complex molecular composition.[25] These proteins mediate firm mechanical stability, serve as a gatekeeper for the paracellular pathway, and help in preserving tissue homeostasis. Dysregulation of cell junction adhesion has been shown to be heavily implicated in the process of EMT.[26] The dysregulation of these junctional proteins is widely correlated in breast, prostate, ovarian, endometrial, lung, liver, and colorectal carcinomas.[27,28] Our single-cell transcriptome analysis revealed that cell-cell junction level decreased and TGFβ-signaling-related EMT program gene expression increased in tumor cells of HBV-ICC.

Immune checkpoints are mechanisms that hamper T cell immune responses. However, immune checkpoint inhibitors (ICIs) release these "brakes" to reactivate T cells to fight against cancer. ICIs offer better treatment responses for advanced ICC patients. Indeed, the degree of T cell infiltration in tumors defines T cell^{high}/hot tumor or T cell^{low}/cold tumor,[29–31] and studies have suggested differential responsiveness toward ICI treatment for hot and cold tumors.[32,33] The presence of tumor-infiltrating lymphocytes (TILs) could predict a better prognosis, indicating the enhancement of tumor T cell infiltration, particularly the CD8 T cells, may provide a potential benefit for patients. Intriguingly, our current study found more CD8 T cells and Th2 cells in HBV-ICC patients. Single-cell transcriptome analysis revealed the immunosuppressive landscape of CD8 T cells in HBV-ICC patients. These findings identify specific molecular targets for subsequent translational applications and provide useful mechanistic information for the future design of efficacious immune-oncology treatments in ICC.

ICAM1, also known as CD54, is a transmembrane glycoprotein in the immunoglobulin superfamily present at basal levels in a wide variety of cell types and is upregulated in response to a number of inflammatory mediators.[34] ICAM1 is also believed to play an important role in several malignancies. In breast, gastric, and colorectal cancers, increased ICAM1 expression in the cancer cells has been correlated with a more favorable prognosis, suggesting a role of ICAM1 in the enhancement of immune surveillance.[35–37] Conversely, potential involvement of ICAM1 expression in cancer invasion and metastasis has been reported in melanoma, breast, gastric, pancreatic, and lung cancers.[38–41] Thus, the biological significance of ICAM1 expression in cancers remains controversial. In our current study, ICAM1 was significantly upregulated in HBV-ICC compare to non-HBV-ICC. The results of our single-cell transcriptome analysis showed that ICAM1 is mainly expressed in TAMs. ICAM1$^+$ TAMs are correlated with a poor prognosis in HBV-ICC, and earlier studies found that ICAM1 acts as a macrophage/cancer-cell adhesion molecule. However, the exact role of ICAM1$^+$ TAMs in ICC progression remains to be elucidated.

To the best of our knowledge, our study is the first to investigate the mechanism of HBV-ICC based on proteomic and single-cell transcriptomic data. Our findings provide insight into the behavior of HBV-infected ICC driven by various pathogenic mechanisms involving decreasing cell-cell junction level and increasing EMT program. The analysis of the immunosuppressive landscape in HBV-ICC provides mechanistic information for the design of efficacious immune-oncology treatments for ICC.
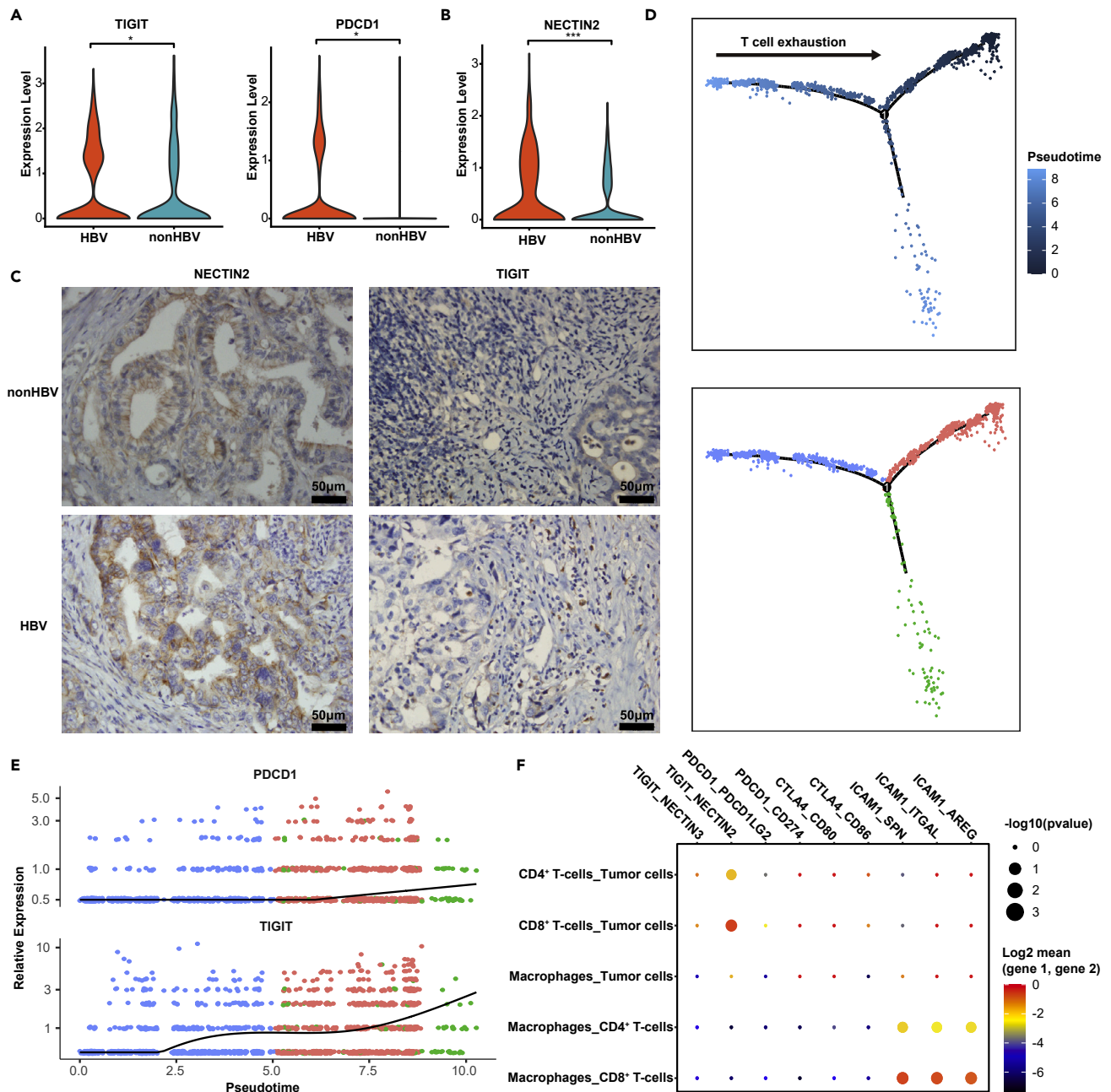
Figure 7. The immunosuppressive landscape of CD8 T cell in HBV-ICC patients

(A) *TIGIT* and *PDCD1* had higher expression levels in the CD8 T cells of HBV-ICC patients.

(B) *NECTIN2* had higher expression levels in tumor cells of HBV-ICC patients.

(C) Representative pictures of NECTIN2 and TIGIT in HBV-ICC and non-HBV-ICC patients by IHC staining. Scale bars, 50 μm.

(D) Pseudotime cell trajectory analysis on CD8 T cells in HBV-ICC samples.

(E) Expression levels of the *PDCD1* and *TIGIT* genes in CD8 T cells along pseudotime.

(F) Immune checkpoint interactions between lymphocytes and APCs (tumor cells and TAMs).

Limitations of the study

Our work has several limitations. First, in this study, although state-of-the-art technologies have been used, roles of ICC have not been rigorously tested by *in vitro* or *in vivo* experiments. Second, the proteomics was done by extracting proteins from the ICC paraffin sections; therefore, the proteins detected are derived from all different cell types. The results will be more reliable if spatial-omics information could be included in the study.

STAR★METHODS

Detailed methods are provided in the online version of this paper and include the following:

- KEY RESOURCES TABLE
- RESOURCE AVAILABILITY
  - Lead contact
  - Materials availability
  - Data and code availability
- EXPERIMENTAL MODEL AND SUBJECT DETAILS
  - Sample collection
- METHOD DETAILS
  - DNA extraction and library preparation
  - Sequencing and analysis for genomic sequencing
  - Tandem mass tag (TMT) -based proteomic analysis
  - Pathway analysis based on proteomic dataset
  - Immune cell deconvolution
  - Tissue dissociation
  - scRNA-seq library preparation and sequencing
  - scRNA-seq data sequencing
  - Cell clustering of scRNA-seq data
  - Determination of major cell types of scRNA-seq data
  - Inference of large-scale CNVs of scRNA-seq data
  - Inferring cell-cycle stage of scRNA-seq data
  - Transcription factor analysis of scRNA-seq data
  - Trajectory inference for cells of scRNA-seq data
  - Cell–cell communication analysis of scRNA-seq data
  - Correlation to public datasets
  - IHC staining for tissue sections
  - Immunofluorescence staining for tissue sections
- QUANTIFICATION AND STATISTICAL ANALYSIS

SUPPLEMENTAL INFORMATION

Supplemental information can be found online at https://doi.org/10.1016/j.isci.2023.106003.

AUTHOR CONTRIBUTIONS

J.R. and P.Z. contributed to study concept and design; C.Y., R.C., Q.L., and S.X. contributed to acquisition of samples and data; Y.S. and S.X. contributed bioinformatics and statistical analysis; Y.S., S.X., M.P.T., J.R., and P.Z. contributed to data interpretation; S.X. and Q.L. contributed to experimental procedures; L.F., W.W., Q.J., Y.J., X.Z., W.F., M.J., and J.C. contributed to discussion of results; Y.S., M.P.T., J.R., and P.Z. contributed to drafting and writing the final manuscript; and J.R. and P.Z. contributed to study supervision.

DECLARATION OF INTERESTS

The authors declare no competing interests.

REFERENCES

1. Bridgewater, J., Galle, P.R., Khan, S.A., Llovet, J.M., Park, J.-W., Patel, T., Pawlik, T.M., and Gores, G.J. (2014). Guidelines for the diagnosis and management of intrahepatic cholangiocarcinoma. J. Hepatol. 60, 1268–1289.

2. Jusakul, A., Cutcutache, I., Yong, C.H., Lim, J.Q., Huang, M.N., Padmanabhan, N., Nellore, V., Kongpetch, S., Ng, A.W.T., Ng, L.M., et al. (2017). Whole-genome and epigenomic landscapes of etiologically distinct subtypes of cholangiocarcinoma. Cancer Discov. 7, 1116–1135.

3. Bertuccio, P., Malvezzi, M., Carioli, G., Hashim, D., Boffetta, P., El-Serag, H.B., La Vecchia, C., and Negri, E. (2019). Global trends in mortality from intrahepatic and extrahepatic cholangiocarcinoma. J. Hepatol. 71, 104–114.

4. Tyson, G.L., and El-Serag, H.B. (2011). Risk factors for cholangiocarcinoma. Hepatology 54, 173–184.

5. Clements, O., Eliahoo, J., Kim, J.U., Taylor-Robinson, S.D., and Khan, S.A. (2020). Risk factors for intrahepatic and extrahepatic cholangiocarcinoma: a systematic review and meta-analysis. J. Hepatol. 72, 95–103.

6. Sung, W.-K., Zheng, H., Li, S., Chen, R., Liu, X., Li, Y., Lee, N.P., Lee, W.H., Ariyaratne, P.N., Tennakoon, C., et al. (2012). Genome-wide survey of recurrent HBV integration in hepatocellular carcinoma. Nat. Genet. 44, 765–769.

7. Jiang, Z., Jhunjhunwala, S., Liu, J., Haverty, P.M., Kennemer, M.I., Guan, Y., Lee, W., Carnevali, P., Stinson, J., Johnson, S., et al. (2012). The effects of hepatitis B virus integration into the genomes of hepatocellular carcinoma patients. Genome Res. 22, 593–601.

8. Amaddeo, G., Cao, Q., Ladeiro, Y., Imbeaud, S., Nault, J.-C., Jaoui, D., Gaston Mathe, Y., Laurent, C., Laurent, A., Bioulac-Sage, P., et al. (2015). Integration of tumour and viral genomic characterisations in HBV-related hepatocellular carcinomas. Gut 64, 820–829.

9. Zou, S., Li, J., Zhou, H., Frech, C., Jiang, X., Chu, J.S.C., Zhao, X., Li, Y., Li, Q., Wang, H., et al. (2014). Mutational landscape of intrahepatic cholangiocarcinoma. Nat. Commun. 5, 5696.

10. An, J., Kim, D., Oh, B., Oh, Y.J., Song, J., Park, N., Kim, H.I., Kang, H.J., Oh, J.H., Kim, W., et al. (2021). Comprehensive characterization of viral integrations and genomic aberrations in HBV-infected intrahepatic cholangiocarcinomas. Hepatology 75, 997–1011.

11. Boerner, T., Drill, E., Pak, L.M., Nguyen, B., Sigel, C.S., Doussot, A., Shin, P., Goldman, D.A., Gonen, M., Allen, P.J., et al. (2021). Genetic determinants of outcome in intrahepatic cholangiocarcinoma. Hepatology 74, 1429–1444.

12. Lowery, M.A., Ptashkin, R., Jordan, E., Berger, M.F., Zehir, A., Capanu, M., Kemeny, N.E., O'Reilly, E.M., El-Dika, I., Jarnagin, W.R., et al. (2018). Comprehensive molecular profiling of intrahepatic and extrahepatic cholangiocarcinomas: potential targets for intervention. Clin. Cancer Res. 24, 4154–4161.

13. Lim, B., Lin, Y., and Navin, N. (2020). Advancing cancer research and medicine with single-cell genomics. Cancer Cell 37, 456–470.

14. Pastushenko, I., Mauri, F., Song, Y., de Cock, F., Meeusen, B., Swedlund, B., Impens, F., Van Haver, D., Opitz, M., Thery, M., et al. (2021). Fat1 deletion promotes hybrid EMT state, tumour stemness and metastasis. Nature 589, 448–455.

15. In Lee, K., and Koval, J.J. (1997). Determination of the best significance level in forward stepwise logistic regression. Commun. Stat. Simulat. Comput. 26, 559–575.

16. Lamouille, S., Xu, J., and Derynck, R. (2014). Molecular mechanisms of epithelial–mesenchymal transition. Nat. Rev. Mol. Cell Biol. 15, 178–196.

17. Pastushenko, I., and Blanpain, C. (2019). EMT transition states during tumor progression and metastasis. Trends Cell Biol. 29, 212–226.

18. Becht, E., McInnes, L., Healy, J., Dutertre, C.-A., Kwok, I.W.H., Ng, L.G., Ginhoux, F., and Newell, E.W. (2019). Dimensionality reduction for visualizing single-cell data using UMAP. Nat. Biotechnol. 37, 38–44.

19. Smith, C.W., Mazharian, A., Thomas, S.G., Raslan, Z., Patel, P., Byrne, M., Lordkipanidzé, M., Bem, D., Meyaard, L., Senis, Y.A., and Watson, S.P. (2017). Mice lacking the inhibitory collagen receptor LAIR-1 exhibit a mild thrombocytosis and hyperactive platelets. Arterioscler. Thromb. Vasc. Biol. 37, 823–835.

20. Meyaard, L., Hurenkamp, J., Clevers, H., Lanier, L.L., and Phillips, J.H. (1999). Leukocyte-associated Ig-like receptor-1 functions as an inhibitory receptor on cytotoxic T cells. J. Immunol. 162, 5800–5804.

21. Maasho, K., Masilamani, M., Valas, R., Basu, S., Coligan, J.E., and Borrego, F. (2005). The inhibitory leukocyte-associated Ig-like receptor-1 (LAIR-1) is expressed at high levels by human naive T cells and inhibits TCR mediated activation. Mol. Immunol. 42, 1521–1530.

22. Cao, Q., Fu, A., Yang, S., He, X., Wang, Y., Zhang, X., Zhou, J., Luan, X., Yu, W., and Xue, J. (2015). Leukocyte-associated immunoglobulin-like receptor-1 expressed in epithelial ovarian cancer cells and involved in cell proliferation and invasion. Biochem. Biophys. Res. Commun. 458, 399–404.

23. Zhang, J., Zhang, Y., Cheng, S., Mu, Y., Liu, Y., Yi, X., Jiang, D., Ding, Y., and Zhuang, R. (2020). LAIR-1 overexpression inhibits epithelial–mesenchymal transition in osteosarcoma via GLUT1-related energy metabolism. World J. Surg. Oncol. 18, 136.

24. Lebbink, R.J., Meyaard, L., de Ruiter, T., Adelmeijer, J., Brenkman, A.B., van Helvoort, J.M., Koch, M., Farndale, R.W., Lisman, T., Sonnenberg, A., and Lenting, P.J. (2006). Collagens are functional, high affinity ligands for the inhibitory immune receptor LAIR-1. J. Exp. Med. 203, 1419–1425.

25. Bhat, A.A., Uppada, S., Achkar, I.W., Hashem, S., Yadav, S.K., Shanmugakonar, M., Al-Naemi, H.A., Haris, M., and Uddin, S. (2018). Tight junction proteins and signaling pathways in cancer and inflammation: a functional crosstalk. Front. Physiol. 9, 1942.

26. Morris, M.A., Young, L.S., and Dawson, C.W. (2008). DNA tumour viruses promote tumour cell invasion and metastasis by deregulating the normal processes of cell adhesion and motility. Eur. J. Cell Biol. 87, 677–697.

27. Martin, T.A., and Jiang, W.G. (2009). Loss of tight junction barrier function and its role in cancer metastasis. Biochim. Biophys. Acta 1788, 872–891.

28. Brennan, K., Offiah, G., McSherry, E.A., and Hopkins, A.M. (2009). Tight junctions: a barrier to the initiation and progression of breast cancer? J. Biomed. Biotechnol. 2010, 1–16.

29. van der Woude, L.L., Gorris, M.A.J., Halilovic, A., Figdor, C.G., and de Vries, I.J.M. (2017). Migrating into the tumor: a roadmap for T cells. Trends Cancer 3, 797–808.

30. Bonaventura, P., Shekarian, T., Alcazer, V., Valladeau-Guilemond, J., Valsesia-Wittmann, S., Amigorena, S., Caux, C., and Depil, S. (2019). Cold tumors: a therapeutic challenge for immunotherapy. Front. Immunol. 10, 168.

31. Vareki, S.M. (2018). High and low mutational burden tumors versus immunologically hot and cold tumors and response to immune checkpoint inhibitors. J. Immunother. Cancer 6, 1–5.

32. Li, J., Byrne, K.T., Yan, F., Taiji, Y., Chen, Z., Timour, B., Richman, L.P., Lin, J.H., Sun, Y.H., and Rech, A.J. (2018). Tumor cell-intrinsic factors underlie heterogeneity of immune cell infiltration and response to immunotherapy. Immunity 49, 178–193.e7.

33. Ribas, A., Dummer, R., Puzanov, I., VanderWalde, A., Andtbacka, R.H.I., Michielin, O., Olszanski, A.J., Malvehy, J., Cebon, J., Fernandez, E., et al. (2017). Oncolytic virotherapy promotes intratumoral T cell infiltration and improves anti-PD-1 immunotherapy. Cell 170, 1109–1119.e10.

34. Roebuck, K.A., and Finnegan, A. (1999). Regulation of intercellular adhesion molecule-1 (CD54) gene expression. J. Leukoc. Biol. 66, 876–888.

35. Fujihara, T., Yashiro, M., Inoue, T., Sawada, T., Kato, Y., Ohira, M., Nishiguchi, Y., shikawa, T., Sowa, M., and Chung, K.H.-Y. (1999). Decrease in ICAM-1 expression on gastric cancer cells is correlated with lymph node metastasis. Gastric Cancer 2, 221–225.

36. Ogawa, Y., Hirakawa, K., Nakata, B., Fujihara, T., Sawada, T., Kato, Y., Yoshikawa, K., and Sowa, M. (1998). Expression of intercellular adhesion molecule-1 in invasive breast cancer reflects low growth potential, negative lymph node involvement, and good prognosis. Clin. Cancer Res. 4, 31–36.

37. Tachimori, A., Yamada, N., Sakate, Y., Yashiro, M., Maeda, K., Ohira, M., Nishino, H., and Hirakawa, K. (2005). Up regulation of ICAM-1 gene expression inhibits tumour growth and liver metastasis in colorectal carcinoma. Eur. J. Cancer 41, 1802–1810.

38. Johnson, J.P., Stade, B.G., Holzmann, B., Schwäble, W., and Riethmüller, G. (1989). De novo expression of intercellular-adhesion molecule 1 in melanoma correlates with increased risk of metastasis. Proc. Natl. Acad. Sci. USA 86, 641–644.

39. Schröder, C., Witzel, I., Müller, V., Krenkel, S., Wirtz, R.M., Jänicke, F., Schumacher, U., and Milde-Langosch, K. (2011). Prognostic value of intercellular adhesion molecule (ICAM)-1 expression in breast cancer. J. Cancer Res. Clin. Oncol. 137, 1193–1201.

40. Koyama, S., Ebihara, T., and Fukao, K. (1992). Expression of intercellular adhesion molecule 1 (ICAM-1) during the development of invasion and/or metastasis of gastric carcinoma. J. Cancer Res. Clin. Oncol. 118, 609–614.

41. Lin, Y.-C., Shun, C.-T., Wu, M.-S., and Chen, C.-C. (2006). A novel anticancer effect of thalidomide: inhibition of intercellular adhesion molecule-1–mediated cell invasion and metastasis through suppression of nuclear factor-κB. Clin. Cancer Res. 12, 7165–7173.

42. Butler, A., Hoffman, P., Smibert, P., Papalexi, E., and Satija, R. (2018). Integrating single-cell transcriptomic data across different conditions, technologies, and species. Nat. Biotechnol. 36, 411–420.

43. Qiu, X., Mao, Q., Tang, Y., Wang, L., Chawla, R., Pliner, H.A., and Trapnell, C. (2017). Reversed graph embedding resolves complex single-cell trajectories. Nat. Methods 14, 979–982.

44. Wu, T., Hu, E., Xu, S., Chen, M., Guo, P., Dai, Z., Feng, T., Zhou, L., Tang, W., Zhan, L., et al. (2021). clusterProfiler 4.0: a universal enrichment tool for interpreting omics data. Innovation 2, 100141.

45. Efremova, M., Vento-Tormo, M., Teichmann, S.A., and Vento-Tormo, R. (2020). CellPhoneDB: inferring cell–cell communication from combined expression of multi-subunit ligand–receptor complexes. Nat. Protoc. 15, 1484–1506.

46. Aibar, S., González-Blas, C.B., Moerman, T., Huynh-Thu, V.A., Imrichova, H., Hulselmans, G., Rambow, F., Marine, J.-C., Geurts, P., Aerts, J., et al. (2017). SCENIC: single-cell regulatory network inference and clustering. Nat. Methods 14, 1083–1086.

47. Aran, D., Hu, Z., and Butte, A.J. (2017). xCell: digitally portraying the tissue cellular heterogeneity landscape. Genome Biol. 18, 220.

48. Tong, L., Ding, N., Tong, X., Li, J., Zhang, Y., Wang, X., Xu, X., Ye, M., Li, C., Wu, X., et al. (2019). Tumor-derived DNA from pleural effusion supernatant as a promising alternative to tumor tissue in genomic profiling of advanced lung cancer. Theranostics 9, 5532–5541.

49. Yang, Z., Yang, N., Ou, Q., Xiang, Y., Jiang, T., Wu, X., Bao, H., Tong, X., Wang, X., and Shao, Y.W. (2018). Investigating novel resistance mechanisms to third-generation EGFR tyrosine kinase inhibitor osimertinib in non-small cell lung cancer patients. Clin. Cancer Res. 24, 3097–3107.

50. Bolger, A.M., Lohse, M., and Usadel, B. (2014). Trimmomatic: a flexible trimmer for Illumina sequence data. Bioinformatics 30, 2114–2120.

51. Li, H. (2013). Aligning sequence reads, clone sequences and assembly contigs with BWA-MEM. Preprint at arXiv. 1303.3997. https://doi.org/10.48550/arXiv.1303.3997.

52. DePristo, M.A., Banks, E., Poplin, R., Garimella, K.V., Maguire, J.R., Hartl, C., Philippakis, A.A., Del Angel, G., Rivas, M.A., Hanna, M., et al. (2011). A framework for variation discovery and genotyping using next-generation DNA sequencing data. Nat. Genet. 43, 491–498.

53. Koboldt, D.C., Zhang, Q., Larson, D.E., Shen, D., McLellan, M.D., Lin, L., Miller, C.A., Mardis, E.R., Ding, L., and Wilson, R.K. (2012). VarScan 2: somatic mutation and copy number alteration discovery in cancer by exome sequencing. Genome Res. 22, 568–576.

54. Fang, W., Ma, Y., Yin, J.C., Hong, S., Zhou, H., Wang, A., Wang, F., Bao, H., Wu, X., Yang, Y., et al. (2019). Comprehensive genomic profiling identifies novel genetic predictors of response to anti–PD-(L) 1 therapies in non–small cell lung cancer. Clin. Cancer Res. 25, 5015–5026.

55. Zhu, Y., Weiss, T., Zhang, Q., Sun, R., Wang, B., Yi, X., Wu, Z., Gao, H., Cai, X., Ruan, G., et al. (2019). High-throughput proteomic analysis of FFPE tissue samples facilitates tumor stratification. Mol. Oncol. 13, 2305–2328.

56. Gao, H., Zhang, F., Liang, S., Zhang, Q., Lyu, M., Qian, L., Liu, W., Ge, W., Chen, C., Yi, X., et al. (2020). Accelerated lysis and proteolytic digestion of biopsy-level fresh-frozen and FFPE tissue samples using pressure cycling technology. J. Proteome Res. 19, 1982–1990.

57. Li, J., Van Vranken, J.G., Pontano Vaites, L., Schweppe, D.K., Huttlin, E.L., Etienne, C., Nandhikonda, P., Viner, R., Robitaille, A.M., Thompson, A.H., et al. (2020). TMTpro reagents: a set of isobaric labeling mass tags enables simultaneous proteome-wide measurements across 16 samples. Nat. Methods 17, 399–404.

58. Shen, B., Yi, X., Sun, Y., Bi, X., Du, J., Zhang, C., Quan, S., Zhang, F., Sun, R., Qian, L., et al. (2020). Proteomic and metabolomic characterization of COVID-19 patient sera. Cell 182, 59–72.e15.

59. Nie, X., Qian, L., Sun, R., Huang, B., Dong, X., Xiao, Q., Zhang, Q., Lu, T., Yue, L., Chen, S., et al. (2021). Multi-organ proteomic landscape of COVID-19 autopsies. Cell 184, 775–791.e14.

60. Hnzelmann, S., Castelo, R., and Guinney, J. (2013). GSVA: gene set variation analysis for microarray and RNA-Seq data. BMC Bioinformatics 14, 7.

61. Büttner, M., Miao, Z., Wolf, F.A., Teichmann, S.A., and Theis, F.J. (2019). A test metric for assessing single-cell RNA-seq batch correction. Nat. Methods 16, 43–49.

62. Sade-Feldman, M., Yizhak, K., Bjorgaard, S.L., Ray, J.P., de Boer, C.G., Jenkins, R.W., Lieb, D.J., Chen, J.H., Frederick, D.T., Barzily-Rokni, M., et al. (2018). Defining T cell states associated with response to checkpoint immunotherapy in melanoma. Cell 175, 998–1013.e20.

63. Tirosh, I., Izar, B., Prakadan, S.M., Wadsworth, M.H., Treacy, D., Trombetta, J.J., Rotem, A., Rodman, C., Lian, C., Murphy, G., et al. (2016). Dissecting the multicellular ecosystem of metastatic melanoma by single-cell RNA-seq. Science 352, 189–196.

64. Jerby-Arnon, L., Shah, P., Cuoco, M.S., Rodman, C., Su, M.-J., Melms, J.C., Leeson, R., Kanodia, A., Mei, S., Lin, J.-R., et al. (2018). A cancer cell program promotes T cell exclusion and resistance to checkpoint blockade. Cell 175, 984–997.e24.

65. Smyth, G.K. (2005). Limma: linear models for microarray data. In Bioinformatics and computational biology solutions using R and Bioconductor (Springer), pp. 397–420.

STAR★METHODS

KEY RESOURCES TABLE

REAGENT or RESOURCE	SOURCE	IDENTIFIER
Antibodies		
Rabbit Polyclonal anti-Nectin-2	Proteintech	Cat#27171-1-AP
Rabbit Monoclonal anti-TIGIT	abcam	Cat#ab243903
Rabbit Polyclonal anti-α-SMA	Proteintech	Cat#55135-1-AP
Mouse Monoclonal anti-CD8a	Proteintech	Cat#66868-1-Ig
Mouse Monoclonal anti-TJP1	Proteintech	Cat#66452-1-Ig
Rabbit Monoclonal anti-CD68	Cell Signaling Technology	Cat#76437
Mouse Monoclonal anti-ICAM-1	Proteintech	Cat#60299-1-Ig
Rabbit Monoclonal anti-CD4	Cell Signaling Technology	Cat#48274S
Mouse Monoclonal anti-GATA3	Proteintech	Cat#66400-1-Ig
Mouse Monoclonal anti-E-cadherin	Proteintech	Cat#60335-1-Ig
Rabbit Polyclonal anti-Vimentin	Proteintech	Cat#10366-1-AP
Biological samples		
Human ICC tissue	This paper	N/A
Deposited data		
ICC transcriptome data	UCSC XENA	https://xena.ucsc.edu/
Software and algorithms		
R (v3.6.2)	R CRAN	https://cran.r-project.org/
Seurat (v3.0.0)	Butler et al., 2018[42]	https://cran.r-project.org/web/packages/Seurat/index.html
Monocle2 (v2.14.0)	Qiu et al., 2017[43]	http://cole-trapnell-lab.github.io/monocle-release/
ClusterProfiler (v4.2.0)	Wu et al., 2021[44]	https://bioconductor.org/packages/release/bioc/html/clusterProfiler.html
CellPhoneDB (v3.0)	Efremova et al., 2020[45]	https://github.com/Teichlab/cellphonedb
SCENIC (v1.2.4)	Aibar et al., 2017[46]	https://github.com/aertslab/SCENIC
xCell	Aran et al., 2017[47]	https://github.com/dviraran/xCell

RESOURCE AVAILABILITY

Lead contact

Further information and requests for resources and reagents should be directed to and will be fulfilled by the lead contact, Prof. Jian Ruan (software233@zju.edu.cn).

Materials availability

This study did not generate new unique reagents.

Data and code availability

The data have been deposited at iProX (Project number: IPX0003037000) and are publicly available as of the date of publication.

This paper does not report original code.

Any additional information required to reanalyze the data reported in this work paper is available from the lead contact upon request.

EXPERIMENTAL MODEL AND SUBJECT DETAILS

Sample collection

This study was approved by the Medical Ethics Committee of the Affiliated Hospital of Southwest Medical University (No. KY2019053) and NanFang Hospital of Southern Medical University (No. NFEC-2021-067 and No. NFEC-2018-028). All participants provided written informed consent to take part in the study. Sample tissues were obtained from the biopsies of 121 patients diagnosed with ICC. All samples were assessed by pathological examinations. The detailed patient information is available in Table S1.

METHOD DETAILS

DNA extraction and library preparation

DNA extraction, library preparation, and target capture enrichment were performed.[48] Briefly, genomic DNA from white blood cells was extracted using the DNeasy Blood & Tissue Kit (Qiagen) and was applied as the normal control to remove germline variations. After deparaffinizing the FFPE samples with xylene, genomic DNA was extracted using the QIAamp DNA FFPE Tissue Kit (Qiagen). After quantification of DNA with Qubit 3.0 using the dsDNA HS Assay Kit (Life Technologies), a Nanodrop 2000 (Thermo Fisher) was used to evaluate the DNA quality. The KAPA Hyper Prep kit (KAPA Biosystems) was used to prepare libraries.[49] Briefly, 1–2 μg of genomic DNA was sheared by a Covaris M220 instrument into ∼350-bp fragments. End repair, A-tailing, and adaptor ligation of fragmented DNA were performed with the KAPA Hyper DNA Library Prep kit (Roche Diagnostics). Agencourt AMPure XP beads (Beckman Coulter) were used for size selection. DNA libraries were generated by polymerase chain reaction (PCR) followed by purification using Agencourt AMPure XP beads. WES was performed with a customized xGen lockdown probe panel (Integrated DNA Technologies). The blocking reagents were human cot-1 DNA (Life Technologies) and xGen Universal Blocking Oligos (Integrated DNA Technologies). Dynabeads M−270 (Life Technologies) and the xGen Lockdown Hybridization and Wash kit (Integrated DNA Technologies) were used to perform the capture reaction. PCR amplification was performed on captured libraries with KAPA HiFi HotStart ReadyMix (KAPA Biosystems). The KAPA Library Quantification kit (KAPA Biosystems) was used to quantify the purified library. Fragment size distribution was determined using an Agilent Bioanalyzer 2100 according to manufacturer's recommendations.

Sequencing and analysis for genomic sequencing

The HiSeq4000 platform (Illumina) was used to generate 2 × 150-bp paired-end sequence reads from the target-enriched libraries. bcl2fastq (v2.19) Conversion software was employed to demultiplex the sequencing data and Trimmomatic[50] was used to remove N and low-quality (quality <15)bases. The alignment of the data to the human reference genome HG19 was then performed by the Burrows-Wheeler Aligner (bwa-mem),[51] followed by further processing using the Picard suite (available at: https://broadinstitute.github.io/picard/) and the Genome Analysis Toolkit (GATK).[52] Single nucleotide polymorphism (SNP) and insertion/deletion (indel) calling for GATK was performed with VarScan2[53] and HaplotypeCaller/UnifiedGenotyper, and the mutant allele frequency (MAF) cutoff was set as 0.5%. Common variants were removed according to dbSNP and the 1000 Genome project. The patients' whole blood controls were used to filter out the germline mutations. TMB was defined as the number of somatic, coding, and base substitution, and indel mutations per megabase of the examined genome DNA, and was calculated.[54] Briefly, all base substitutions were considered, including nonsynonymous and synonymous alterations, and indels in the coding region of targeted genes, with the exception of mutations in known hotspots in oncogenic driver genes and truncations in tumor suppressors.

Tandem mass tag (TMT) -based proteomic analysis

Formalin-fixed paraffin-embedded (FFPE) samples (0.5–1 mg) were dewaxed and rehydrated and then subjected to acidic hydrolysis with formic acid (FA). Proteins were denatured with 6 M urea (Sigma-Aldrich, Germany) and 2 M thiourea (Sigma-Aldrich, Germany), and then digested into peptides with trypsin (1:20, Hualishi, Beijing, China) and Lys-C (1:80, Hualishi, Beijing, China) with the assistance of pressure-cycling technology (PCT).[55,56] Peptides were labeled with TMTpro™ 16 plex (Thermo Fisher Scientific™, San Jose, USA).[57] Each batch contained 15 experimental samples and one pooled sample in the TMT126 channel for normalization. The fractions (60 per batch) were separated using offline high-pH reversed-phase chromatography with a Thermo Dionex Ultimate 3000 RSLCnano System and then combined to a total of 30 fractions per batch. Subsequently, the fractionated samples were separated with a Thermo Dionex Ultimate 3000 RSLCnano System and then analyzed with a Q Exactive HF mass

spectrometer using the data-dependent acquisition (DDA) mode (Thermo Fisher Scientific™, San Jose, USA). The database searching included all reviewed human entries from UniProt (downloaded on 14 April 2020, containing 20,365 proteins) using Proteome Discoverer (version 2.4, Thermo Fisher Scientific™, Waltham, MA).[58,59]

Pathway analysis based on proteomic dataset

DEP of cell subgroups were recognized by the DESeq2. |FC| > 2 and q value (false discovery rate) < 0.05 were used as the cut-off criteria. GO enrichment analysis was performed on these DEPs with R package clusterProfiler.[44] Single-sample GSEA (ssGSEA) was applied to evaluate the enrichment scores of each sample. ssGSEA was conducted with the R package GSVA.[60] The REACTOME gene sets were downloaded from The Broad Institute.

Immune cell deconvolution

xCell[47] is a webtool that performs cell type enrichment analysis from gene expression data for 64 immune and stroma cell types. xCell is a gene signatures-based method learned from thousands of pure cell types from various sources. We applied xCell to the proteomic datasets with the gene signature to estimate the relative fractions of immune cell types and epithelial cells.

Tissue dissociation

RPMI 1640 (Gibco, Cat. no. 11875–093, US) containing1 mM protease inhibitor (Solarbio, Cat. no. P6730, China), was used to transport ICC tissues. Tissues were digested with a dissociation enzyme cocktail prepared by dissolving 2 mg/mL Dispase II (Sigma-Aldrich, Cat.42613-33-2 US), 1 mg/mL Type VIII Collagenase (Sigma-Aldrich, Cat. no. C2139, US), and 1 unit/mL DNase I (NEB, Cat. no. M0303S, US) in PBS with 5% fetal bovine serum (FBS; Gibco, Cat. no. 16000–044, US) for 40 min at 37°C. The cells were dissociated and collected every 20 min, and then filtered using a 40 μm nylon cell strainer (Falcon, Cat. no. 352340, US). Red blood cell lysis buffer (Invitrogen, Cat. US) with 1 unit/mL DNase I was used to remove red blood cells. Finally, the cells were washed in PBS with 0.04% BSA (BSA; Sigma-Aldrich, Cat. no. B2064, US).

scRNA-seq library preparation and sequencing

The concentration of the single-cell suspension was computed with a Countess™ Automated Cell Counter (Thermo) and adjusted to 1000 cells/μL. Cells were loaded according to the Chromium single-cell 3′ kit standard protocol to capture 5,000–10,000 cells/chip position (V2 chemistry). The library construction and all subsequent procedures were performed according to the manufacturer's standard protocol.

scRNA-seq data sequencing

Illumina HiSeq X Ten was used to obtain single-cell libraries using 150 nt paired-end sequencing.

Cell Ranger (version 2.2.0) was used to process the raw data, demultiplex cellular barcodes, map reads to the transcriptome, and down-sample reads (as required to generate normalized aggregate data across samples). These process produced a raw unique molecular identifier (UMI) count matrix, which was converted into a Seurat object by the R package Seurat[42] (version 3.0.0). Cells with UMI numbers <1000 or with over 10% mitochondrial-derived UMI counts were considered low-quality cells and were removed. In order to eliminate potential doublets, single cells with over 6000 genes detected were also filtered out. Following removal of the poor-quality cells and doublets, a total of 18,171 cells were retained for downstream analyses. Library size normalization was performed in Seurat on the filtered gene–cell matrix to obtain the normalized UMI (unique molecular identifier) count data. Statistical assessment of possible batch effects was performed using the R package k-BET (a robust and sensitive k-nearest neighbor batch-effect test).[61] k-BET was run on major immune cell types including B, CD4 and CD8 T cells separately with default parameters. A control dataset with known significant batch effects was included to assist with data interpretation. We chose the k input value from 1% to 100% of the sample size. In each run, the number of tested neighborhoods was 10% of the sample size. The mean and maximal rejection rates were then calculated based on a total of 100 repeated k-BET runs. A low rejection rate indicates homogeneous mixing of samples from different batches. k-BET results suggested minimal batch effects in this dataset.

Cell clustering of scRNA-seq data

Seurat was applied to the normalized gene–cell matrix to identify highly variable genes for unsupervised cell clustering. To identify highly variable genes, the MeanVarPlot method in the Seurat package was used to establish the mean–variance relationship of the normalized counts of each gene across cells. To reduce the dimensionality of the scRNA-Seq dataset, principal component analysis (PCA) was performed on an integrated data matrix. The top 30 PCs were used to perform the downstream analysis using the Elbowplot function of Seurat. The main cell clusters were identified with the FindClusters function of Seurat, with resolution set as default (res = 0.8). Clusters were were visualized with 2D tSNE or UMAP plots.

Determination of major cell types of scRNA-seq data

To define the major cell type of each single cell, differentially expressed genes (DEGs) were identified for each cell cluster using the FindAllMarkers analysis in the Seurat package and the top 30 most significant DEGs were carefully reviewed. In parallel, feature plots were generated for the top 30 DEGs and a suggested set of canonical immune and stromal cell markers followed by a manual review process.[62] Enrichment of these markers (for example, EPCAM for epithelial cells, PTPRC for immune cells, CD3D/E for T cells, CD8A/B for CD8 T cells, IL7R/CD4/CD40LG for CD4 T cells, CD19/MS4A1/CD79A for B cells, COL1A1/COL1A2 for fibroblasts, and so on) in certain clusters was considered a strong indication of the clusters representing the corresponding cell types. The two approaches were combined to infer major cell types for each cell cluster according to the enrichment of marker genes and top-ranked DEGs in each cell cluster.[62]

Inference of large-scale CNVs of scRNA-seq data

The tool inferCNV (https://github.com/broadinstitute/inferCNV) was applied to infer the large-scale CNVs from scRNA-seq data, and monocytes from this dataset were used as a control for CNV analysis. Initial CNVs were estimated by sorting the analyzed genes by their chromosomal locations and applying a moving average to the relative expression values, with a sliding window of 100 genes within each chromosome.[63] Finally, malignant cells were distinguished from normal cells based on the information integrated from multiple sources, including cluster distribution of the cells, marker gene expression, inferred large-scale CNVs and aneuploidy status.

Inferring cell-cycle stage of scRNA-seq data

The cell-cycle stage was computationally assigned for each individual cell by the function CellCycleScoring that is implemented in Seurat. Cell-cycle stage was inferred based on the expression profile of the cell-cycle-related signature genes.[64]

Transcription factor analysis of scRNA-seq data

SCENIC[46] is a computational method used in the construction of regulatory networks and in the identification of different cell states from scRNA-seq data. To measure the difference between HBV-ICC and nonHBV-ICC tumor cells based on transcription factors or their target genes, SCENIC was performed on all single cells, and the preferentially expressed regulons were calculated by the Limma package.[65] Only regulons significantly upregulated or downregulated in at least one cluster, with adj. p value <0.05, were involved in further analysis.

Trajectory inference for cells of scRNA-seq data

To map differentiation in the TME, pseudotime analysis was performed with Monocle2[43] in order to determine the dramatic translational relationships among cell types and clusters. Further detection with the Monocle2 plot_pseudotime_heatmap function revealed the key role of a series of genes in the differentiation progress. Significantly changed genes were identified by the differential GeneTest function in Monocle2 with a q-value <0.01.

Cell–cell communication analysis of scRNA-seq data

CellPhoneDB[45] is a Python-based computational analysis tool which enables analysis of cell–cell communication at the molecular level. A website version was also provided for analysis of a relatively small dataset (http://www.cellphonedb.org/). Single cells that were clustered into different cell types were investigated using the software to determine interaction networks. Interaction pairs have p-values <0.05 returned by CellPhoneDB, were selected for the evaluation of relationships between cell types.

Correlation to public datasets

Transcriptome data from The Cancer Genome Atlas (TCGA) ICC datasets were obtained from UCSC XENA (https://xena.ucsc.edu/). Clinical information was obtained from cBioPortal (https://www.cbioportal.org/).

IHC staining for tissue sections

Tumor tissues were fixed with 4% (v/v) paraformaldehyde before embedding them in paraffin. Tissue sections (4 μm) were later deparaffinized with xylene and rehydrated in a graded alcohol concentration series. Antigen epitope retrieval was induced by microwave heating. Tissue sections were then blocked for 1h, at room temperature, in goat serum blocking solution (Proteintech, B900780, China) and PBS (PBS). Tissue samples were incubated with primary antibody overnight at 4°C and the following day tissue the samples were stained using an anti-mouse/rabbit universal immunohistochemical detection kit (pk10006, proteintech) following the manufacturer's instructions. Mounted sections were examined by light microscopy (Leica), and images were analyzed with Image-Pro Plus 448 (version 6.0).

Immunofluorescence staining for tissue sections

Tissue samples were deparaffinized with xylene and rehydrated with graded alcohol concentration series. Antigen epitope retrieval was induced by microwave heating. Tissue sections were permeabilized with 0.2% 452 Triton X-100 and then blocked with 5% BSA, for 1h, at room temperature, and then incubated with the primary antibody, overnight, at 4°C. The following day, tissue sections were washed with PBS three times. Samples were then stained with fluorescent secondary antibodies (Invitrogen, USA) in the dark, for 1h, at room temperature, and then washed with PBS three times before mounting them onto slides using Mowoil supplemented with DPAI to stain the nucleus. Finally, a confocal microscope (Nikon, Japan) was used to take images of ICCA tissue samples and the acquired images were analyzed using ImageJ (version 4.0).

QUANTIFICATION AND STATISTICAL ANALYSIS

Fisher's exact tests (nonparametric) and Chi-square tests (parametric) were used to assess the associations of categorical variables, while the Wilcoxon rank-sum test (nonparametric) and Student's t test (parametric) were used to assess the associations of continuous variables. Kaplan–Meier estimates with log rank tests among strata, and Cox proportional-hazards regression models were employed to analyze survival data. Survival analysis was performed with the ''survival'' package.